A 40-million-year history of atmospheric CO₂

Journal:	*Philosophical Transactions A*
Manuscript ID:	RSTA-2013-0096
Article Type:	Research
Date Submitted by the Author:	31-Jan-2013
Complete List of Authors:	Zhang, Yi Ge; Yale University, Department of Geology and Geophysics Pagani, Mark; Yale University, Department of Geology and Geophysics Liu, Zhonghui; The University of Hong Kong, Department of Earth Sciences Bohaty, Steven; National Oceanography Centre, University of Southampton, Ocean and Earth Science DeConto, Robert; University of Massachusetts-Amherst, Department of Geosciences
Issue Code: Click here to find the code for your issue.:	DM1011
Subject:	Climatology < EARTH SCIENCES, Geochemistry < EARTH SCIENCES, Oceanography < EARTH SCIENCES
Keywords:	Cenozoic carbon dioxide, alkenone-pCO2 method, carbon isotopes, benthic oxygen isotopes, global temperature, cryosphere

SCHOLARONE™
Manuscripts

1 # A 40-million-year history of atmospheric CO_2

2 Yi Ge Zhang[1†], Mark Pagani[1], Zhonghui Liu[2], Steven M. Bohaty[3], and Robert DeConto[4]

3

4 [1]Department of Geology and Geophysics, Yale University, New Haven, Connecticut
5 06520-8109, USA
6 [2]Department of Earth Sciences, The University of Hong Kong, Hong Kong, China
7 [3]Ocean and Earth Science, National Oceanography Centre, University of Southampton,
8 Southampton SO14 3ZH, UK
9 [4]Department of Geosciences, University of Massachusetts-Amherst, Amherst,
10 Massachusetts 01003, USA

11

12

13

14 [†]Corresponding Author:
15 210 Whitney Ave, New Haven, Connecticut 06520-8109
16 yige.zhang@yale.edu; +1 203 823 5495

17

Submitted to Phil. Trans. R. Soc. A - Issue

Page 2 of 39

18 **Abstract**

19   The alkenone-pCO$_2$ methodology has been used to reconstruct the partial pressure of

20 ancient atmospheric carbon dioxide (pCO$_2$) for the past 45 million years of Earth's

21 history (middle Eocene to Pleistocene epochs). The current long-term CO$_2$ record is a

22 composite of data from multiple ocean localities that express a wide range of

23 oceanographic and algal-growth conditions that potentially bias CO$_2$ results. In this study

24 we present a pCO$_2$ record spanning the past 40 million years from a single marine locality,

25 Ocean Drilling Program Site 925 located in the western equatorial Atlantic Ocean. The

26 trends and absolute values of our new CO$_2$ record site are broadly consistent with

27 previously published multi-site alkenone-CO$_2$ results. However, new pCO$_2$ estimates for

28 the middle Miocene are notably higher than published records, with average pCO$_2$

29 concentrations in the range of 400-500 ppm. Our results are generally consistent with

30 recent pCO$_2$ estimates based on boron isotope-pH data and stomatal index records, and

31 suggest that CO$_2$ levels were highest during a period of global warmth associated with the

32 Middle Miocene Climatic Optimum (17-14 million years ago, Ma), followed by a decline

33 in CO$_2$ during the Middle Miocene Climate Transition (~14 Ma). Several relationships

34 remain contrary to expectations. For example, benthic foraminiferal δ^{18}O records suggest

35 a period of deglaciation and/or high-latitude warming during the latest Oligocene (27-23

36 Ma) that, based on our results, occurred concurrently with a long-term decrease in CO$_2$

37 levels. Additionally, a large positive δ^{18}O excursion near the Oligocene/Miocene

38 boundary (the Mi-1 event, ~23 Ma), assumed to represent a period of glacial advance and

39 retreat on Antarctica, is difficult to explain by our CO$_2$ record alone given what is known

40 of Antarctic ice sheet history and the strong hysteresis of the East Antarctic Ice Sheet

41 once it has grown to continental dimensions. We also demonstrate that in the Neogene

42 with low CO$_2$ levels, algal carbon concentrating mechanisms and spontaneous

43 biocarbonate-CO$_2$ conversions are likely to play a more important role in algal carbon

44 fixation, which provides a potential bias to the alkenone-pCO$_2$ method.

45

46   **Key Words:** Cenozoic carbon dioxide; alkenone-pCO$_2$ method; carbon isotopes; benthic

47   oxygen isotopes; global temperature; cryosphere

48

1. Introduction

49

50   Knowledge of the partial pressure of atmospheric CO_2 (pCO_2), beyond direct

51 measurements of atmospheric- [1] and ice-core gas compositions over the last 800

52 thousand years [2-4], derive from a range of techniques including stomatal indices of

53 fossil leaves (e.g. [5-9]), the carbon isotopic compositions of paleosol carbonate nodules

54 (e.g. [10-12]), the boron isotopic compositions of shallow-dwelling foraminifera (e.g.

55 [13-17]), and the stable carbon isotope compositions of algal biomarkers, such as

56 alkenones (e.g. [18-24]). Most Cenozoic CO_2 reconstructions indicate substantially

57 higher CO_2 values in the early Eocene with a broad decrease during the middle Eocene

58 into the Neogene. However, a two-fold variation in absolute pCO_2 concentrations persists

59 among the available proxies during key climatic intervals [25].

60   Following the initial development of alkenone–based CO_2 reconstructions for the

61 Pleistocene and Holocene [26, 27], a revised methodology was applied for long-term CO_2

62 reconstructions for the middle Eocene to the Pleistocene [18-20, 22, 23, 28]. More than

63 twenty marine localities have been used for Cenozoic reconstructions. However, the

64 published Cenozoic alkenone CO_2 record represents a stacked record from various ocean

65 localities (e.g. [28]). This potentially introduces bias into CO_2 trends and magnitudes

66 because temperature, nutrient conditions, seasonality and thermocline depth can impact

67 algal growth conditions and contribute to variability in reconstructed CO_2 estimates. Thus,

68 temporal CO_2 patterns from composite records could have trends specific to individual

69 sites and not representative of changes in long-term global atmospheric conditions [21].

70   In this study, we present a continuous alkenone-based CO_2 record from one marine

71 site for the past 40 million years in order to limit variability introduced by composite

72 results. With this new record we attempt to reconcile the discrepancy of CO_2 level

73 reconstructions between alkenone and other proxies, and explore CO_2 forcing in the

74 context of global climate change since the late middle Eocene. Also discussed is a

75 preliminary assessment of the potential bias related to algal carbon concentrating

- 4 -

Page 5 of 39

Submitted to Phil. Trans. R. Soc. A - Issue

76 mechanisms (CCMs) and spontaneous bicarbonate-CO_2 conversion, when using the

77 alkenone-pCO_2 method to estimate CO_2 levels in the Cenozoic.

78 **2. Background**

79 **2.1 The Alkenone-pCO_2 method**

80 **2.1.1 Diffusion versus active carbon uptake models of carbon transport**

81   Alkenones occur as a suite of long-chained (C_{37}-C_{39}) unsaturated ethyl and methyl

82 ketones produced by a few haptophyte algae in the modern ocean [29, 30]. Today, the

83 predominant sources of alkenones derive from *Emiliania huxleyi* (originating in the Late

84 Pleistocene; [31]) and *Gephyrocapsa oceanica* (originating in the Pliocene; [32]).

85 Sedimentary alkenones that pre-date the Pliocene were likely produced by haptophytes

86 related to the family *Noelaerhabdaceae* and genera *Reticulofenestra* and *Dictyococcites*

87 [33-37].

88   Alkenone-based pCO_2 reconstructions require paired measurements on stable

89 carbon-isotope composition of the di-unsaturated C_{37} methyl ketone ($\delta^{13}C_{37:2}$) and

90 carbonates. Differences between the $\delta^{13}C$ of algal carbon and carbonate represent the

91 total carbon isotope fractionation (ε_p) that occurs during algal growth. ε_p derived from

92 $\delta^{13}C_{37:2}$ values ($\varepsilon_{p37:2}$) is calculated by the equation:

93     $$\varepsilon_{p37:2} = \left[\frac{\delta_{CO_{2(aq)}} + 1000}{\delta_{org} + 1000} - 1 \right] \times 1000 \qquad \text{Equation 1}$$

94 where δ_{org} is the carbon isotopic composition of the algal cell estimated from the $\delta^{13}C$ of

95 alkenone ($\delta_{37:2}$). The isotopic difference between δ_{org} and $\delta_{37:2}$ is 4.2‰, following the

96 work of [26, 27, 38]:

97     $$\delta_{org} = \left[(\delta_{37:2} + 1000) \times \left(\left(\frac{4.2}{1000} \right) + 1 \right) \right] - 1000 \qquad \text{Equation 2}$$

98 $\delta_{CO_{2(aq)}}$ is the $\delta^{13}C$ value of dissolved $CO_{2(aq)}$ approximated from the $\delta^{13}C$ values of

99 shallow-dwelling foraminifera assuming isotopic and chemical equilibria among all

100   inorganic carbon species, atmospheric CO_2, and foraminifera calcite tests (e.g. [26]).

101   The alkenone-CO_2 method is based on the assumption that the transport of inorganic

102   carbon (dissolved CO_2) across the cell membrane to the site of carbon fixation within the

103   algal cell predominantly occurs by diffusion. For diffusion transport, the total stable

104   carbon isotope fractionation that occurs during marine photosynthesis is described by the

105   equation [39, 40]:

106      $$\varepsilon_p = \varepsilon_t + (\varepsilon_f - \varepsilon_t)\left(\frac{C_i}{C_e}\right) \hspace{4cm} \text{Equation 3}$$

107   where C_e represents the ambient concentration of $CO_{2(aq)}$ ($[CO_{2(aq)}]$), C_i is the intracellular

108    $[CO_{2(aq)}]$, ε_f is the total carbon isotope fractionation that occurs during photosynthesis,

109   and ε_t is the carbon isotope fractionation associated with carbon transport. Most

110   alkenone-based pCO_2 reconstructions have adopted a range of ε_f values from 25 to 28‰

111   (e.g. [18-20, 22-24]), consistent with the majority of algal growth experiments [41, 42].

112   Chemostat incubations for two strains of alkenone-producing haptophyte algae and

113   two diatoms, under continuous light and nitrate-limited conditions show that ε_p linearly

114   varies with $[CO_{2(aq)}]$, specific growth rate (μ), and cell geometry [42-44], consistent with

115   a predominantly diffusion carbon transport model. In contrast, dilute batch cultures of *E.*

116   *huxleyi* grown under nutrient-replete conditions and variable irradiance yield lower $\varepsilon_{p37:2}$

117   values, minor response to $[CO_{2(aq)}]$ changes [45], and an irradiance effect on the

118   magnitude of $\varepsilon_{p37:2}$ [46]. Such results suggest that assumptions of a strictly diffusion

119   carbon uptake model may not be valid under some nutrient and light conditions. For

120   example, low $[CO_{2(aq)}]$ chemostat experiments for diatom *P. tricornutum* resulted in a

121   nonlinear response of ε_p to $\mu/[CO_{2(aq)}]$, indicating that a carbon concentrating mechanism

122   (CCM) was triggered when the supply of $CO_{2(aq)}$ became limiting to growth (in this case,

123    $< \sim 7$ μmol kg^{-1}, [44, 47]). CCMs are known to be available to a broad range of algal

124   species [48-51]. However, whether or not ancient alkenone producing algae were

125   characterized by CCMs is presently unknown.

126   **2.1.2 Simplified model of diffusion carbon uptake and paleoclimate reconstructions**

127   Various physiological factors have been shown to impact C_i (Equation 3, [52]).

128   However, because C_i is difficult to constrain, Jasper and Hayes (1994) recast Equation 3

129   as [26]:

130    $$\varepsilon_p = \varepsilon_f - \frac{b}{[CO_2]}$$ Equation 4

131   where the term '*b*' represents a range of physiological variables that encompass the

132   combined effects of growth rate, cell geometry and other potential factors.

133   Surface-water analysis of $\delta^{13}C_{37:2}$ and seawater chemistry show a strong relationship

134   between '*b*' in Equation 4 and the concentration of soluble phosphate [21, 53]. Dissolved

135   reactive phosphate ($[PO_4^{3-}]$) is a key macronutrient that often co-varies with other

136   biolimiting trace-metal micronutrients such as iron, zinc and cobalt [53], providing a link

137   between $[PO_4^{3-}]$, growth rate and the value of ε_p.

138   Calibration of '*b*' with respect to $[PO_4^{3-}]$ using all available data (see [21] for

139   references) results in the following relationships assuming $\varepsilon_f = 25‰$:

140    $$b = (118.52 \times [PO_4^{3-}]) + 84.07$$ Equation 5

141   **2.1.3 Uncertainties in pCO$_2$ calculations**

142   If carbon assimilation is primarily determined by diffusion transport, ε_p is well

143   described by Equation 3. However, various other parameters, in addition to $CO_{2(aq)}$, are

144   known to play a role in the expression of ε_p. Some of these parameters influence ε_p

145   through a direct impact on C_i including growth rate, irradiance, cell membrane

146   permeability, and cell size. CO_2 estimates are further compromised by uncertainties in

147   phosphate concentrations used to estimate the physiological-dependent term '*b*', as well

148   as the potential of regionally different '*b*' versus $[PO_4^{3-}]$ relationships relative to the

149   global calibration. Assumptions regarding the value of enzymatic isotope fractionation

150   (ε_f), as well as knowledge of sea surface temperatures (SSTs) – generally obtained from

151   various geochemical proxies, further contribute to CO_2 uncertainties. [21]. Finally, other

152   factors, such as CCMs, likely arise when the intracellular concentration of CO_2 becomes

Submitted to Phil. Trans. R. Soc. A - Issue

Page 8 of 39

153   limiting. CCMs can impact the value of ε_p by transporting different carbon species with

154   specific carbon isotopic compositions, and altering C_i relative to diffusive flux. Also,

155   isotope fractionations associated with active transport mechanisms are likely distinct.

156   **2.2 Site location**

157   Ocean Drilling Program (ODP) Site 925 (4°12.25'N, 43°29.33'W, 3042 m water

158   depth) is located on Ceara Rise in the western equatorial Atlantic Ocean (Figure 1, [54]).

159   Modern surface waters at this site are characterized by high mean annual SST (~27.5°C)

160   and low nutrient levels (surface $[PO_4^{3-}]$ ~ 0.14 μmol/L, [55]). The middle Eocene to

161   Pleistocene sedimentary succession recovered at Site 925 consists of pelagic carbonate

162   oozes and chalks, primarily foraminifer-bearing nannofossil oozes with minor amounts of

163   clay. All samples used in this study were taken from ODP Hole 925A. Previously

164   reported Plio-Pleistocene pCO$_2$ data are based on Hole 925C and 925D [22].

165   Paleogeographic reconstructions indicate that this site has moved northward over the

166   past 40 Ma, from just south of the equator during the late Eocene, to ~ 4°N today (Figure

167   1, [56]). Site 925 was right on the equator around 30 Ma. Available mass accumulation

168   rates of biogenic barium and reactive phosphorous suggest stable productivity and

169   nutrient conditions from 36.9 to 32.7 Ma [57]. Calcareous nannofossils indicate weak to

170   moderate tropical upwelling history [54] consistent with a minor air-sea CO$_2$

171   disequilibrium expressed today, with modern surface waters enriched by ~22 ppm [58].

172   **3. Methods**

173   **3.1 Lipid extraction and analysis**

174   Approximately 40 to 100 grams of sediment (dry weight) were used for biomarker

175   analysis. Samples were freeze-dried and extracted with dichloromethane/methanol (2:1,

176   v/v) using an Accelerated Solvent Extractor (ASE 300, Dionex) at 120°C and 10.3 MPa.

177   Total lipid extracts (TLEs) were concentrated under a stream of purified N$_2$ using a

- 8 -

178 Zymark Turbovap II and then separated into three fractions using silica gel

179 chromatography. TLEs were separated into compound classes using ashed Pasteur

180 pipettes loaded with ~4g deactivated silica gel (70-230 mesh), and sequentially eluted

181 with 2 ml hexane, 4 ml dichloromethane, and 4 ml of methanol to obtain aliphatic,

182 aromatic, and polar fractions, respectively.

183 The dichloromethane fraction containing ketones was subject to basic hydrolysis and

184 silver nitrate column chromatography to purify long-chain alkenones. Relative

185 abundances of di- and tri-unsaturated methyl ketones were analyzed on a Thermo Trace

186 2000 GC equipped with an Rxi-1ms column (60 m × 0.25 mm × 0.25 μm), a pressure-

187 and temperature-variable (PTV) injector and a flame ionization device (FID) with He as

188 the carrier gas. The oven was set to 90°C upon sample injection, held for 1 min, ramped

189 up at 20°C/min to 280°C, then 2°C /min to 320°C. Temperature was held constant at

190 320°C for 30 min. The relative abundance of C37:2 and C37:3 alkenones were used to

191 compute $U_{37}^{k\prime}$, a proxy developed to reconstruct ancient SSTs [59, 60]. Analytical

192 precision, determined through multiple analyses of an in-house alkenone standard,

193 represents an uncertainty of ±0.005 $U_{37}^{k\prime}$ units (Supplementary Material).

194 The methanol fraction containing glycerol dialkyl glycerol tetraethers (GDGTs) was

195 further purified by passing through activated alumina dissolved in

196 dichloromethane/methanol (1:1, v/v). The eluting fraction was dried under pure N_2

197 stream, then dissolved in an azeotrope of hexane/isopropanol (99:1, v/v) and filtered

198 through and ashed 0.7 µm glass microfiber filter. Analyses of GDGTs were conducted

199 following a slightly modified method described by [61]. Compound identification and

200 relative abundance analyses were determined using an Agilent 1200 high performance

201 liquid chromatography/atmospheric pressure chemical ionization – mass spectrometer

202 (HPLC/APCI-MS). Separation of GDGTs was archived on an Alltech Prevail cyano

203 column (150 mm, 2.1 mm I.D., and 3 µm grain size) kept at 30°C. The following solvent

204 polarity gradient was used, based on A: hexane/isopropanol (99:1, v/v), and B:

205   hexane/isopropanol (90:10, v/v): 100% solvent A for 5 min, then solvent B was linearly

206   increased from 0% at 5 min, to 7.4% at 40 min, and maintained from 40 to 50 min. After

207   each sample analysis the column was back flushed with 100% solvent B for 14 min,

208   followed by 10 min equilibration with normal phase flow of 100% solvent A. Mass

209   spectrometric identification and quantification were achieved using an Agilent 6130 ion

210   trap mass spectrometer coupled to the HPLC by an APCI interface. Ion scans were set to

211   *m/z* 1200-1500. Quantification was based on peak intensities in the mass chromatogram

212   of the $[M+H]^+$ ions. Relative abundance of GDGTs was used to calculate TEX_{86}, a proxy

213   employed to estimate past SSTs [62]. Repeated measurements of an in-house laboratory

214   standard showed the analytical precision represented ±0.01 TEX_{86} units (Supplementary

215   Material).

216   **3.2 Carbon Isotope Measurements**

217   Carbon isotopic compositions of $C_{37:2}$ alkenones were analyzed on a Thermo

218   Finnigan MAT 253 mass spectrometer interfaced with a Trace GC Combustion III

219   (GC-IRMS) equipped with a PTV injector and a J&W Scientific DB-1 capillary column

220   (60 m × 0.25 mm × 0.25 mm), using He as a carrier gas with a flow speed of 2.0 mL

221   min^{-1}. GC temperature was held at 60°C for 1 minute, increased to 320°C at 15°C/min,

222   and held isothermally for 35 minutes. Carbon isotopes are reported relative to the VPDB

223   standard based on an in-house reference gas calibrated to the OzTech standard ($\delta^{13}C$ =

224   -40.61‰). A C_{20} *n*-alkane standard was injected daily to determine the analytical

225   accuracy of the carbon isotope measurements, yielding an uncertainty of ±0.2‰. $U_{37}^{k\prime}$

226   and $\delta^{13}C_{37:2}$ data reported for the Eocene-Oligocene climate transition [21] and the

227   Pliocene to Pleistocene [22] have been previously published (Supplementary Material).

228   **3.3 Foraminifera Stable Isotope Measurements**

229   Splits of samples were wet-sieved with deionized water at 63 μm. Surface-dwelling

230   planktic foraminifera, including *Globigerinoides ruber, 'Globigerinoides ruber* s.1.', and

Page 11 of 39

Submitted to Phil. Trans. R. Soc. A - Issue

231   *Globigerinoides altiaperturus,* were picked from the 250-300 μm sieve fraction in the

232   Neogene section, and epifaunnal benthic foraminifera (*Cibicidoides* spp.) were picked

233   from the >250 μm sieve fraction throughout the entire Site 925 study section. Carbon

234   stable isotope analysis of the picked foraminiferal samples was performed using a Europa

235   GEO 20-20 mass spectrometer at the University of Southampton. Samples were reacted

236   with phosphoric acid at 70°C using an automatic carbonate preparation system "CAPS"

237   in line with the mass spectrometer. Typically, 5 to 8 benthic specimens from each sample

238   were combined and analyzed together, and 15 to 20 planktic specimens were analyzed

239   together. All values are reported relative to the VPDB scale, with an external analytical

240   precision estimated at 0.08‰ for $\delta^{13}C$ (Supplementary Material).

241   **3.4 Chronology**

242   Age determinations for ODP Hole 925A are based on biostratigraphy planktic

243   foraminifera ([63, 64]) with 75 age control points based on first and last occurrence

244   datums (Supplementary Material) over the a span of 40 million years. All datums are

245   calibrated to the Geomagnetic Polarity Timescale (GPTS) of [65] and the integrated

246   timescale of Berggren et al. (1995) [66].

247   **4. Results**

248   **4.1 Temperature**

249   Sea surface temperatures based on $U_{37}^{k\prime}$ and TEX_{86} indices were reconstructed for

250   the past 40 Ma using the linear calibration of [67] and the reciprocal calibration of [68],

251   respectively (Figure 2A). $U_{37}^{k\prime}$ SST reconstructions indicate relatively constant

252   temperatures of ~28°C since the late Eocene, except for a ~2°C cooling during the

253   Pliocene-Pleistocene interval. However, 28.3°C represents maximum temperatures

254   expressed by the $U_{37}^{k\prime}$ calibration ($U_{37}^{k\prime}$ value reaches 1), and therefore warmer

255   temperatures above ~28°C cannot be determined. In contrast, maximum temperatures

256   associated with the TEX_{86} proxy are unconstrained. Reconstructed TEX_{86} records exhibit

Submitted to Phil. Trans. R. Soc. A - Issue

Page 12 of 39

257   much larger fluctuations compared to $U_{37}^{k\prime}$ with temperatures of ~30°C in the late

258   Eocene that fall to ~22°C during the late Pliocene — more than 5°C cooler at the same

259   locality today. However, the TEX_{86}-based temperatures since Pliocene might suffer from

260   additional GDGT inputs, as indicated by high BIT values (mean value is 0.6,

261   Supplementary Material) [69].

262   In order to estimate CO_2, we do not favor one SST proxy over the other for the

263   entire 40 million year record from Site 925. Instead, we selected the highest temperature

264   estimates from both $U_{37}^{k\prime}$ and TEX_{86} records to synthesize a composite temperature

265   profile. Differences between $U_{37}^{k\prime}$ and TEX_{86} records are considered to reflect the

266   uncertainty of SST reconstructions at each sample, which is further utilized in the

267   computation of $\varepsilon_{p37:2}$ and pCO_2. We also realize that different calibrations for $U_{37}^{k\prime}$- and

268   TEX_{86}-SST conversion could introduce additional uncertainties, but they are secondary

269   compared to the difference between the two proxies themselves.

270   **4.2 Carbon isotopes and $\varepsilon_{p37:2}$**

271   Planktonic foraminifera are partially to fully recrystallized in the upper Eocene-lower

272   Oligocene interval of Site 925. $\delta^{13}C$ measurements on the presumed surface-water

273   dwellers *Turborotalia* spp. show only small differences (0.1-0.5‰) from the benthic

274   *Cibicidoides* spp. within the same sample, suggesting that *Turborotalia* either maintained

275   a thermocline habitat or is affected by diagenetic alteration [21]. However, agreement

276   between *Cibicidoides* $\delta^{13}C$ values at Site 925 and an Eocene-Oligocene Southern Ocean

277   compilation of $\delta^{13}C$ values from ODP Sites 689, 733, 744 and 748 suggests adequate

278   preservation of $\delta^{13}C$ values [21]. Consequently, Pagani et al. (2011) reconstructed surface

279    $\delta^{13}C$ by measuring *Cibicidoidis* $\delta^{13}C$ values, assuming a constant offset (0.94‰) between

280   surface- and deep-waters $\delta^{13}C_{DIC}$ [21].

281   Miocene mixed-layer foraminifera are better preserved than Paleogene specimens.

282   *Globogerinoides altiaperturus* were measured in the early Miocene and *Globogerinoides*

283   *ruber* s.1. or *G. ruber* s.1. were selected in the mid- to late-Miocene interval. A $\delta^{13}C$

284   offset of 0.94‰ with an ascribed uncertainty of ±0.3‰ [70] was applied to both *G. ruber*

285   and *G. altiaperturus* $\delta^{13}C$ values to estimate surface-water $\delta^{13}C_{DIC}$ (Figure 2B). The

286   planktic foraminifera approach in the Miocene is accompanied by benthic foraminifera

287   *Cibicidoides* $\delta^{13}C$ analyses and the applications of assumed surface-deep water isotopic

288   offsets. Results show that the two independent approaches are within 0.20‰ from each

289   other (Supplementary Material). Carbon isotope compositions on the shallow-dwelling

290   *Globogerinoides sacculifer* since 5 Ma have been previously reported (Figure 2B, [22]).

291        $\delta^{13}C_{37:2}$ values are more ^{13}C-depleted during the Paleogene relative to the Neogene

292   (Figure 2C). Calculation of $\delta^{13}C$ of surface seawater aqueous CO_2 is by converting the

293   mixed-layer $\delta^{13}C_{DIC}$ (Figure 2B), using the composite temperature estimates and

294   associated uncertainties from organic geochemical proxies (Section 4.1), assuming

295   equilibrium isotopic fractionations between different carbonate species. Aqueous CO_2

296    $\delta^{13}C$ and $\delta^{13}C_{37:2}$ are further used to calculate $\varepsilon_{p37:2}$.

297   Figure 2 shows that variability in $\delta^{13}C_{37:2}$ is predominantly responsible for the

298   character of $\varepsilon_{p37:2}$ trends. $\varepsilon_{p37:2}$ values exhibit a long-term decreasing trend, with the

299   majority of $\varepsilon_{p37:2}$ varying between 21-18‰ during the late Eocene to early Oligocene,

300   16-13‰ in the late Oligocene/Miocene, and 13-11‰ during the Pliocene/Pleistocene

301   (Figure 2D).

302   **4.3 pCO_2 Estimates**

303   We assume a value of 25‰ for ε_f [41, 42, 44], and a range of $[PO_4^{3-}]$ from 0.14 μM

304   to 0.39 μM, representing the present-day phosphate concentrations from 0 m to 100 m

305   near Site 925 [55], with 50 m (0.20 μM) to be the most representative depth for alkenone

306   production. Estimates of pCO_2 were then calculated assuming air – sea equilibrium and

307   proxy temperatures (the composite temperature, see Section 4.1) using Henry's law

308   (Figure 2E). The uncertainty of pCO_2 is constrained by the variability of temperature and

309   phosphate estimates. The maximum pCO_2 is calculated by using the upper limit of the ε_p,

310   highest phosphate level, and highest temprature estimates; whereas the mimimum of

311   pCO_2 is a result of the lower limit of ε_p, lowest phosphate, and lowest temperature (See

312   Sections 4.1 and 4.2 for the determination of uncertainties associated with temperature

313   and ε_p). The resulting uncertainty of pCO_2 estimates averages 38%, much larger than an

314   error propagation model through Monte Carlo procedure (11%) with assumed uncertainty

315   of different parameters used in pCO_2 calculations [20].

316   **5. Discussion**

317   **5.1 Comparisons between Site 925 and published Cenozoic pCO_2 records**

318   Our new CO_2 results from Site 925 (Figure 3 and 4) broadly agree with previously

319   published composite alkenone- pCO_2 record for the Cenozoic [28]. Nevertheless,

320   systematic differences are apparent with the new record indicating higher CO_2 levels after

321   ~32 Ma (Figure 3). This discrepancy can be explained, in part, by regional differences in

322   oceanography and algal growth conditions, as expressed by variable ε_p values. For

323   example, the Miocene average ε_p at Site 925 is ~15‰, significantly higher than the mean

324   value of ~10‰ at Deep Sea Drilling Project (DSDP) Site 588 [19, 20]. Further, new SST

325   estimates (e.g. [19, 20]) are used in this study and these new $U_{37}^{k\prime}$- and TEX_{86}-based

326   temperature records are considerably warmer during the Miocene to early Pliocene,

327   compared to foraminifer $\delta^{18}O$-based estimates (6-8°C, DSDP Site 588, [22]). Warmer

328   SST estimates increase calculated pCO_2 levels [22].

329   Finally, comparison of our new record with recent CO_2 reconstruction efforts, with

330   putatively improved techniques and higher quality data [25] suggests broad agreement

331   with boron isotope-pH [13, 15, 16], stomata- [5-9] and paleosol estimates [10-12],

332   although paleosol estimates have inherently larger uncertainties (Figure 4).

333   **5.2 Paleoclimate implications**

334   **5.2.1 The late middle Eocene to early Oligocene**

Page 15 of 39

Submitted to Phil. Trans. R. Soc. A - Issue

335 Coupled climate – ice sheet model simulations of the Eocene/Oligocene climate

336 transition indicate that sudden non-linear jumps in ice volume can be triggered by the

337 congruence of favorable orbital cycles when pCO_2 concentrations decrease to 2.5 to 3

338 times preindustrial levels (~750 ppm, Figure 5, [71, 72]). Independent proxy

339 reconstructions of pCO_2 across the Eocene/Oligocene transition, including those

340 estimated by the boron isotope-pH methodology [16] and alkenone-based CO_2 records

341 from Site 925 [21], support these model results and suggest CO_2 began to decrease

342 immediately prior to the Oi-1 event and declined during the climate transition, likely

343 falling below the ~750 ppm threshold.

344 Compared to a multi-site approach, oceanography and algal growth conditions might

345 be less variable in a single site. However, the late Eocene – early Oligocene CO_2 record

346 at Site 925 may still carry features that are specific to this locality. Although no major

347 tropical upwelling has been detected throughout the entire record by calcareous

348 nannofossil assemblages [54], plate reconstructions indicate that Site 925 tectonically

349 moved from the Southern to the Northern Hemisphere and was positioned on the equator

350 around 30 Ma (Figure 1). This transit would have altered the expression of local

351 sea-surface CO_2, particularly at the equator where the convergence of trade winds drives

352 upwelling of CO_2-rich deep waters [73]. A distinct spike in ε_p values and reconstructed

353 pCO_2 is evident in the middle Oligocene (~29.5 Ma, Figure 2D), representing about

354 10-30% increase of CO_2 from the background level. The magnitude of present-day

355 equatorial upwelling, however, is represented by a seawater CO_2 enrichment in the

356 western equatorial Atlantic by ~30 ppm — about 9% deviation from

357 atmosphere-seawater equilibrium [58]. This potentially implies that equatorial upwelling

358 only partially contributed to the middle Oligocene pCO_2 spike recorded in Site 925, or

359 that upwelling intensity was higher and/or upper water-column stratification was less

360 intense during the Oligocene.

361 **5.2.2 The late Oligocene to early Miocene**

362   Climatic behavior during the late Oligocene/early Miocene interval is particularly

363 difficult to explain given existing CO_2 records. After a period of gradual cooling

364 following the onset of glaciation on Antarctica near the Eocene/Oligocene climate

365 transition at ~34 Ma, an ~0.8‰ decrease in benthic $\delta^{18}O$ values (ODP 1218, eastern

366 equatorial Pacific, [74]) suggest a period of substantial warming and/or deglaciation

367 during the latest Oligocene (~27-23 Ma, Figure 5). However, our corresponding CO_2

368 records indicate a long-term decrease in atmospheric carbon dioxide through the late

369 Oligocene (Figure 5). Isotopic evidence for warming and or partial deglaciation at the end

370 of the Oligocene is not simply an artifact of stacked benthic $\delta^{18}O$ records from different

371 marine sites [74, 75] given that the $\delta^{18}O$ record from ODP Site 1218 spans the entire

372 Oligocene and unambiguously supports the presence of a negative oxygen isotope

373 excursion during this time [74]. Thus, the cause for this negative $\delta^{18}O$ trend remains

374 unresolved in relation to our new CO_2 record.

375   Another apparent decoupling between CO_2 and climate occurs near the

376 Oligocene-Miocene boundary (~23 Ma), represented by a transient, positive benthic

377 foraminiferal $\delta^{18}O$ excursion (>1‰) interpreted as a period of substantial glaciation

378 (known as the Mi-1 event, [76]). Our records suggest invariant CO_2 concentrations during

379 this of apparent glaciation/deglaciation, defying our current understanding of the

380 necessary forcing required to drive Antarctic ice sheet variability.

381   Assuming ~2°C of cooling in the deep sea [77], ~0.5‰ of the ~1‰ $\delta^{18}O$ shift at

382 Mi-1 must have been driven by an increase in ice volume. If continental ice on Antarctica

383 had an average isotopic composition of -40‰, as indicated by isotopic modeling [72],

384 then more than 22×10^6 km^3 of ice — roughly equivalent to the entire present day East

385 Antarctic Ice Sheet (EAIS) — must have accumulated within 400 thousand years.

386 However, CO_2 levels during the Oligocene appear low enough to have already

387 maintained a fully glaciated Antarctica according to ice sheet simulations [78]. Moreover,

388 the recovery phase of Mi-1 is even more enigmatic because models require substantially

- 16 -

389 higher CO_2 levels — at least two-times higher than the formation threshold of the EAIS

390 (~1500 ppm) to cause substantial ice sheet retreat [72, 78]. Coupled climate-ice sheet

391 simulations show that orbital forcing alone cannot cause Antarctic deglaciation once the

392 ice sheet expands over the continent [71], and requires increases in greenhouse gas

393 concentrations to more than 4 times preindustrial levels to cause substantial ice retreat

394 [78]. It is possible that the resolution of our new CO_2 record is too low to resolve large

395 fluctuations within the body of the Mi-1 event. Still, exiting the glacial period would

396 require substantially higher CO_2 levels that are not detected in our record. Alternatively,

397 polar climate sensitivity to CO_2 might have been much higher than simulated in climate

398 models, or our understanding of Antarctic ice physics is incomplete and ice sheet stability,

399 potentially reflected by the 'Oi' and 'Mi' events (e.g. [74]), is far more sensitive and

400 dynamic than indicated in modeling studies. Another possibility is that the assumption

401 that benthic $\delta^{18}O$ variability is representative of global temperature/ice volume is flawed.

402 For example, Nd isotope records suggest alternating deepwater sources during the

403 Paleogene [79, 80], with the potential to alter the temperature, salinity, and $\delta^{18}O$ value of

404 deep waters. Different deep-water sources during the late Oligocene and the Mi-1 event

405 could have played a role in the magnitude of the observed benthic $\delta^{18}O$ fluctuations.

406   Apparent discrepancies between proxy records of ice volume and CO_2 could also

407 result if alkenone CO_2 estimates are simply incorrect or biased for some time intervals.

408 Various theoretical and empirical exercises have been performed to assess non-CO_2

409 factors that impact algal carbon isotope fractionation and uncertainties in alkenone-pCO_2

410 estimations [50, 52]. For example, higher ambient CO_2 levels during the earlier part of

411 the Cenozoic could have contributed to a reduction in bicarbonate uptake via

412 β-carboxylation, resulting in ε_f values greater than 25‰ [21], as well as inhibiting carbon

413 concentrating mechanisms (CCMs). The isotopic impact of CCM up-regulation during

414 low CO_2 would arguably minimize ε_p and reconstructed CO_2 variability, which is

415 discussed in greater detail in Section 5.3.

Submitted to Phil. Trans. R. Soc. A - Issue

Page 18 of 39

5.2.3 The Mid- to Late-Miocene

Very low Miocene pCO_2 concentrations that characterize published alkenone (Figure 3, [19, 20]) and boron-isotope [81] CO_2 records have puzzled the paleoclimate community for nearly a decade. If atmospheric CO_2 was a key parameter forcing cryosphere expansion during the Neogene, major Northern Hemisphere glaciation should have arguably occurred some 20 million years earlier than the accepted age of ~2.7 Ma (Figure 3, [72, 82, 83]). Low pCO_2 levels are also difficult to reconcile with the well-documented warmth of the middle and late Miocene, which was characterized by SSTs significantly higher than today [84]. For example, subtropical east Pacific (ODP 1010) and northeast Pacific (ODP 1021) have been found to be at least 12°C warmer at 12 Ma relative to today, and 5°C warmer relative to the early Pliocene [84]. Prior alkenone and boron isotope reconstructions have both indicated that the global warmth of the middle Miocene climate optimum (MMCO, ~17-14 Ma) and the subsequent expansion and stabilization of Antarctic ice sheets (middle Miocene climate transition, MMCT, ~14 Ma) were associated with relatively invariant pCO_2 [20, 81] and slightly higher pCO_2 during ice expansion (Figure 3, [20]). Not surprisingly, climate models applying published alkenone and boron-isotope-based CO_2 records [85, 86] cannot simulate middle Miocene climate signals as determined by proxy records [19, 81].

Intriguingly, our new record implicates a more important role for pCO_2 in the climatic variability of the early to middle Miocene. The partial pressure of carbon dioxide rises to 400 to 500 ppm during the climatic optimum of the middle Miocene followed by an ~100 ppm decline during MMCT (Figure 5), which better agrees with recent stomatal index [6] and boron isotope estimates (Figure 4, [15]). Comparing the Site 925 record to the earlier alkenone-pCO_2 record from DSDP Site 588 [19, 20], we found that the isotopic fractionation $\varepsilon_{p37:2}$ is larger (15‰ versus 10‰) and the SST estimate is higher by 6-8°C, both of which could have contributed to higher Miocene CO_2 levels in the new assessment. Although we cannot rule out the possibility that CO_2 air – sea disequilibrium

Page 19 of 39

Submitted to Phil. Trans. R. Soc. A - Issue

443   at Site 925 contributed to higher local CO_2 estimates, three independent methods agree

444   that pCO_2 during the MMCO was higher, and then declined during the MMCT cooling,

445   implying that CO_2 was closely linked to major Miocene climate events. Importantly,

446   Miocene CO_2 levels now appear higher than Pliocene and Pleistocene concentrations,

447   consistent with the appearance of Northern Hemisphere glaciation during the Pliocene

448   (Figures 3, 5).

5.3 Assessing the effect of bicarbonate-CO_2 conversion

450   The capacity for active carbon transport is common among marine and fresh water

451   algae [48, 49, 51]. This is because RUBISCO, the primary carboxylase, has a relatively

452   low affinity for CO_2 and, for most algal species, is less than half saturated under current

453   CO_2 levels [51]. CCMs increase carbon availability and reduce rates of photorespiration

454   that impact rates of carbon fixation [51].

455   Whether or not CCMs were an important aspect of ancient alkenone-producers

456   remains speculative. Whereas some organisms, such as diatoms, show highly efficient

457   and active CCMs [48, 87], CCMs in modern *E. huxleyi* and other coccolithophores

458   appear weakly expressed [53, 88]. Physiological parameters of extinct

459   alkenone-producing species are unknown. Since CCMs are energetically expensive,

460   ancient haptophytes probably lacked operational CCMs under the significantly higher

461   CO_2 levels of the past [89]. However, the presence of CCMs could have become more

462   pronounced during the Neogene due to the considerable decline in atmospheric CO_2

463   (Figure 3, 4, 5, and 6). If this perspective is valid, quantitative CO_2 reconstructions could

464   be compromised during periods of relatively low pCO_2 levels.

465   Various theoretical models have been developed to understand the factors that would

466   drive up-regulation of CCMs [47, 50, 90, 91]. One model assumes that active transport

467   occurs when diffusive flux achieves a minimum threshold of intracellular CO_2 necessary

468   for adequate growth. Minimum diffusive flux estimates depend on ambient $[CO_{2(aq)}]$ and

469   constraints imposed by cell size. Assuming spherical geometry, minimum $[CO_{2(aq)}]$ can be

470   defined as [47, 90, 91]:

471    $$[CO_2]_{min} = \frac{F_{in}}{4\pi r D_T (1+r/r_k)}$$ Equation 6

472   where F_{in} is the diffusive influx of $CO_{2(aq)}$, D_T is the diffusion coefficient of CO_2, r is the

473   "surface area equivalent" spherical cell radius [91], r_k is the reacto-diffusive length (i.e,

474   length of the boundary layer where HCO_3^- has the opportunity to convert to CO_{2aq}), and

475   the term $(1+r/r_k)$ represents the contribution of extracellular, uncatalyzed and spontaneous

476   HCO_3^--$CO_{2(aq)}$ conversion to the total supply of CO_2 [47, 90].

477   The term r_k is calculated by

478    $$r_k = \sqrt{\frac{D_T}{k'}}$$ Equation 7

479   where k' is the rate constant for conversion of HCO_3^- and H_2CO_3 to $CO_{2(aq)}$. An

480   approximation for the temperature dependence of D_T is given by [92] that

481    $$D_T = 5.019 \times 10^{-6} e^{-\left(\frac{E_d}{RT_K}\right)}$$ Equation 8

482   with activation energy E_d = 19510 J mol^{-1}, gas constant R = 8.3143 J K mol^{-1}, and T_K is

483   temperature in degrees Kelvin. For the rate constant k', Gavis and Ferguson (1975)

484   demonstrated that

485    $$k' = k_1[OH^-] + k_2$$ Equation 9

486   where k_1 and k_2 are the rate constants of formation of CO_2 from HCO_3^- and H_2CO_3,

487   respectively, and $[OH^-]$, the hydroxyl ion concentration. At 25°C, k_1 = 8500 m^3 mol^{-1} s^{-1},

488   k_2 = 3×10^{-5} s^{-1} [93].

489   Given the equilibrium constant for seawater $K_w = [H^+][OH^-]$, $[OH^-]$ can be

490   calculated if seawater pH is known. At atmospheric pressure [94]:

491    $$\ln K_w^* = 148.96502 - \frac{13847.26}{T_K} - 23.6521\ln T_K$$

492    $$+ \left[\frac{118.67}{T_K} - 5.977 + 1.0495\ln T_K\right] S^{1/2} - 0.01615 S$$ Equation 10

493   Therefore, the portion of fixed CO_2 contributed by the conversion from bicarbonates in

494   the geological past can be calculated if seawater temperature (T_K), pH, salinity (S), and

495   the cell size (r) of ancient alkenone-producers are constrained.

496   Ocean pH estimates and SST reconstructions are available for the Eocene –

497 Oligocene climate transition [16], middle Miocene [15], Pliocene [18] and the

498 Pleistocene [13], and ancient cell sizes for assumed alkenone producers (e.g.

499 *Reticulofenestra, Dictyococcites* and *Cyclicargolithus*) can be estimated using coccolith

500 size measurements [21, 37, 89, 95]. However, the available coccolith length data and

501 boron-based pH estimates are not derived from the same marine sites. Cell sizes of

502 assumed alkenone-producers show large spatial variability. For example, Pagani et al.

503 (2011) demonstrated that *Reticulofenestrid* coccoliths from the Southern Ocean sites (e.g.

504 ODP 1090) were two times as large as those in the tropical Atlantic (ODP 925, 929)

505 during the E-O transition. This apparent cell size variability of alkenone-producers

506 hampers the application of available coccolith data to the HCO_3^- - CO_2 conversion

507 evaluation of the Cenozoic. Therefore, given that cell size data for the past 40 million

508 years is not available for Site 925, we assume a constant cell radius of 2.67 μm, which is

509 the average value estimated from coccolith dimensions for the Cenozoic [21, 37, 89].

510   Boron isotope-derived seawater pH and coeval Mg/Ca-based SST, with the

511 assumption of a constant salinity of 35 and 2.67 μm cell radius of alkenone-producers,

512 enables an assessment of the impact of bicarbonate-CO_2 conversion on alkenone-pCO_2

513 estimates during the Cenozoic. Temporal patterns in the ratio r/r_k indicate that the

514 percentage of fixed carbon derived from bicarbonate conversion is generally low, on the

515 order of 1.4-2.3% (Figure 7), with a trend of elevated bicarbonate contribution by the

516 Pleistocene (~40% more relative to the late Eocene; Figure 7). Since we assume constant

517 cell size, this increase is primarily due to an ~0.5 pH drop from ~7.7 during the latest

518 Eocene [16] to 8.2 today. Alternatively, CCMs could have become increasingly important

519 [50, 96] to counter low CO_2. However, accurate quantitative correction for the effect of

520 HCO_3^- - CO_2 conversion on alkenone-pCO_2 estimates will require more detailed

521 site-specific data on cell size of the alkenone-producers and pH history of the region.

522   An alternative model to estimate CCM activity (Laws et al. 1997; 2002) considers

Submitted to Phil. Trans. R. Soc. A - Issue

Page 22 of 39

523 both diffusion and active uptake of inorganic carbon to describe the non-linear culture

524 results of *P. tricornutum*:

525
$$\varepsilon_p = \varepsilon_f + \varepsilon_t - \varepsilon_{-t} - \left(\frac{1}{1+\frac{C_eP}{\mu C(1+\beta)}}\right)\left(\frac{\varepsilon_f-\varepsilon_{-t}}{\beta+1}\right)$$
Equation 11

526 Here, β is a constant equivalent to the ratio of CO_2 loss (leakage by diffusion) to carbon

527 fixation, P is membrane permeability, C is cell carbon content, and ε_{-t} is the isotopic

528 fractionation associated with the inorganic carbon diffusion back from the cell, to the

529 surrounding seawater. As detailed in Laws et al. (2002), the value of ε_p becomes

530 insensitive to $\mu/[CO_{2(aq)}]$ when:

531
$$\frac{\mu}{C_e} \geq \frac{P}{C(1+\beta)}$$
Equation 12

532 Empirical relationships between P and C show its dependence on the cell radius: P/C =

533 0.285/r. Minimum $[CO_{2(aq)}]$ that would trigger active transport occurs when the term (1+

534 β) approaches unity, or leakage is zero. Laws et al. (2002) calculate that ε_p for *E. huxleyi*

535 would become a non-linear function of $\mu/[CO_{2(aq)}]$ as photoperiod growth rate exceeds

536 1.1 d^{-1} for a cell radius of 2.6 µm, comparable to the culture results of *E. huxleyi* [42].

537   Growth rates in the natural environment for *E. huxleyi* and other alkenone-producing

538 haptophytes are generally low, below 1 d^{-1}, ranging from 0.1 to 1 d^{-1} [53, 97]. Cell

539 dimensions of alkenone-producing algae since middle Eocene [18, 21, 37, 89] used in

540 conjunction with estimates of pCO$_2$ provides a means to identify geologic intervals when

541 up-regulation of CCMs was potentially necessary. For example, cell radii for alkenone

542 producers range from ~4 to 2.4 µm during the Eocene – Oligocene transition [21], and

543 cell radii were about 50% smaller during the early Miocene [37]. Knowledge of cell

544 radius allows calculation of the ratio P/C [50] and the ratio $\mu/[CO_{2(aq)}]$ can be estimated

545 from alkenone-based CO$_2$ reconstructions and a range of modern haptophyte growth rates,

546 assuming alkenone-based CO$_2$ estimates are valid even if CCMs were active. Using pCO$_2$

547 data from earlier results [19, 20, 28], Figure 7 shows that for low to moderate growth

548 rates, the operation of CCMs is expected during the Miocene, particularly during the

Page 23 of 39

Submitted to Phil. Trans. R. Soc. A - Issue

549 climatic optimum of the late early Miocene, suggesting that the alkenone-CO_2 estimates

550 may be compromised during this time interval. Obviously, this result is speculative given

551 the necessary assumptions. For example, CO_2 concentrations used in this exercise derive

552 from alkenone measurements and if CCMs were active, then these CO_2 values would

553 appear artificially lower than actual concentrations and further exaggerate the potential

554 influence of CCMs.

555 **Conclusions**

556   An alkenone-based pCO_2 record spanning the past 40 million years is presented for

557 ODP Site 925 – representing the first long-term Cenozoic pCO_2 record constructed from

558 a single site. Facilitated by improved methodology and careful consideration of

559 assumptions, this record provides refined pCO_2 estimates from a site that is characterized

560 by limited long-term variability in oceanographic conditions. This record, therefore,

561 reflects our most up-to-date effort to better constrain the Cenozoic history of atmospheric

562 CO_2. This new record confirms predictions from climate models regarding the role of

563 CO_2 in the cryosphere evolution in both hemispheres at several key time intervals (e.g.

564 Eocene – Oligocene transition, MMCT, Plio-Pleistocene). This record also suggests that

565 Miocene CO_2 levels were higher than earlier estimates, which better reconciles a

566 long-standing data – model discrepancy for the Miocene. However, outstanding issues

567 remain which include the presumed warming or deglaciation in the late Oligocene and

568 the abrupt and transient oxygen isotope excursion at Mi-1, both of which challenge our

569 understanding of CO_2 climate and ice sheet sensitivity.

570   We also evaluate spontaneous $HCO_3^- $-$CO_{2(aq)}$ conversion, which is one variable that

571 could impact CO_2 estimates from the alkenone-pCO_2 method. We conclude that the

572 contribution from $HCO_3^- $-$CO_2$ conversion to the carbon fixed by alkenone-producing

573 algae is minor, although this potential has increased by 40% from late Eocene to the

574 Quaternary. Finally, an exercise to evaluate potential CCM activity in haptophyte algae

575 suggest that low pCO_2 levels in the Neogene is more likely to trigger CCM mechanisms.

576   **Acknowledgements**

580

- 24 -

581   **Figure Captions**

582   Figure 1. Global plate reconstruction shows the location of ODP Site 925 at 40 Ma, 20

583   Ma, and the present, as well as a detail of the northward movement of Site 925 since 40

584   Ma [56]. Continents are shown as tectonic terrains rather than shorelines.

585

586   Figure 2. Time series of ODP Site 925. (A) $U^{k\prime}_{37}$ and TEX_{86} based SST reconstruction;

587   (B) Adjusted carbon isotopes from foraminiferal stable isotope measurements to

588   proximate $\delta^{13}C$ of surface water dissolved inorganic carbon. (C) Carbon isotopes of

589   alkenones; (D) $\varepsilon_{p37:2}$ calculated from (B) and (C); (E) pCO_2 calculated from (D), using

590   both $U^{k\prime}_{37}$ and TEX_{86} based SST estimates, and assuming $[PO_4^{3-}]$ values were 0.20, 0.14

591   (lower limit) and 0.39 μM (upper limit). Refer to Supplementary Material to see details

592   of constructing (B), (D), (E) and their related uncertainties; One CO_2 estimate at 35.52

593   Ma give value > 2400 ppm, which is off the chart and therefore not shown in the

594   following figures.

595

596   Figure 3. A comparison of alkenone-based pCO_2 composite from multiple marine sites as

597   compiled in [28] and ODP Site 925 record since the late Eocene. Antarctic glaciation

598   thresholds (~750 ppm) and Northern Hemisphere glaciation threshold (~280 ppm)

599   deduced from climate models [72] are marked by dashed lines.

600

601   Figure 4. Comparison between different proxy-based pCO_2 estimates for the past 40 Ma.

602   Boron isotope, paleosol and stomata data are summarized by [25], with additional data

603   from Foster et al. (2012) [15].

604

605   Figure 5. Climate and atmospheric CO_2 history for the past 40 Ma. Benthic $\delta^{18}O$ from

606   [75]. Major warming (red arrows) and cooling (blue arrows) events are labeled. Red bars

607   indicate brief history of Antarctic and Northern Hemisphere ice sheets. Antarctic

608   glaciation thresholds (~750 ppm) and Northern Hemisphere glaciation threshold (~280

609   ppm) deduced from climate models [72] are marked by dashed lines.

610

611   Figure 6. Comparison between the spontaneous bicarbonate-$CO_{2(aq)}$ conversion (green

612   symbols) and the CCM potential of alkenone producers (orange bands) for the past 45 Ma.

613   $HCO_3^- - CO_{2(aq)}$ conversion (r/r_k) based on the model of Riebesell et al. (1993) and

614   Wolf-Gladrow et al., (1997) [90, 91], using seawater pH and SST data provided by boron

615   isotope studies [13, 15, 16, 18], and a constant radius of 2.67 μm for alkenone-producing

616   haptophyte algae. Computation of CCM potential is based on the model of [44, 50],

617   utilizing previously published cell size [21, 37, 89, 95] and existing paleo-CO_2 estimates

618   [18, 21, 28]. CCM potential ($[(\mu/C_e)/(/P/C)]100 - 100$) represents an arbitrary, qualitative

619   scale of CCM activity.

620

Page 27 of 39

Submitted to Phil. Trans. R. Soc. A - Issue

References

1. Keeling, C.D., The concentration and isotopic abundances of carbon dioxide in the atmosphere. *Tellus*, 1960. **12**: p. 200-203,

2. Petit, J.R., et al., Climate and atmospheric history of the past 420,000 years from the Vostok ice core, Antarctica. *Nature*, 1999. **399**: p. 429-436, DOI: 10.1038/20859.

3. Luthi, D., et al., High-resolution carbon dioxide concentration record 650,000-800,000 years before present. *Nature*, 2008. **453**: p. 379-382, DOI: 10.1038/nature06949.

4. Siegenthaler, U., et al., Stable carbon cycle-climate relationship during the late Pleistocene. *Science*, 2005. **310**: p. 1313-1317, DOI: 10.1126/science.1120130.

5. van der Burgh, J., H. Visscher, D.L. Dilcher, and W.M. Kurschner, Paleoatmospheric signatures in Neogene fossil leaves. *Science*, 1993. **260**: p. 1788-1790,

6. Kurschner, W.M., Z. Kvacek, and D.L. Dilcher, The impact of Miocene atmospheric carbon dioxide fluctuations on climate and evolution of terrestrial ecosystems. *Proc. Natl. Acad. Sci.*, 2008. **105**: p. 449-453,

7. Kurschner, W.M., Leaf stomata as biosensors of paleoatmospheric CO_2 levels. *LPP Contributions Series* 1996. **5**: p. 1-153,

8. Royer, D.L., Stomatal density and stomatal index as indicators of paleoatmospheric CO_2 concentration. *Rev. Palaeobot. Palynology*, 2001. **114**: p. 1-28, DOI: 10.1016/s0034-6667(00)00074-9.

9. Retallack, G.J., Greenhouse crises of the past 300 million years. *GSA Bull.*, 2009. **121**: p. 1441-1455,

10. Ekart, D.D., T.E. Cerling, I.P. Montanez, and N.J. Tobor, A 400 million year carbon isotope record of pedogenic carbonates: implications for paleoatmospheric carbon dioxide. *Am. J. Sci.*, 1999. **299**: p. 805-827,

11. Retallack, G.J., Refining a pedogenic-carbonate CO_2 paleobarometer to quantify a middle Miocene greenhouse spike. *Palaeogeogr. Palaeoclimatol. Palaeoecol.*, 2009. **281**: p. 57-65,

12. Cerling, T.E., Use of carbon isotopes in paleosols as an indicator of the $p(CO_2)$ of the paleoatmosphere. *Global Biogeochem. Cyc.*, 1992. **6**: p. 307-314,

13. Honisch, B., G.N. Hemming, D. Archer, M. Siddall, and J.F. McManus, Atmospheric carbon dioxide concentration across the mid-Pleistocene transition. *Science*, 2009. **324**: p. 1551-1554,

14. Bartoli, G., B. Honisch, and R.E. Zeebe, Atmospheric CO_2 decline during the Pliocene intensification of Northern Hemisphere glaciation. *Paleoceanography*, 2011. **26**, DOI: doi:10.1029/2010PA002055.

15. Foster, G.L., C.H. Lear, and J.W.B. Rae, The evolution of pCO_2, ice volume and climate during the middle Miocene. *Earth Planet. Sci. Lett.*, 2012. **341-344**: p. 243-254,

16. Pearson, P.N., G.L. Foster, and B.S. Wade, Atmospheric carbon dioxide through the Eocene-Oligocene climate transition. *Nature*, 2009. **461**: p. 1110-U204, DOI: 10.1038/nature08447.

17. Sanyal, A., N.G. Hemming, G.N. Hanson, and W.S. Broecker, Evidence for a higher pH in the

Submitted to Phil. Trans. R. Soc. A - Issue

Page 28 of 39

661   glacial ocean from boron isotopes in foraminifera. *Nature*, 1995. **373**: p. 234-236,

662   18.   Seki, O., G.L. Foster, D.N. Schmidt, A. Mackensen, K. Kawamura, and R.D. Pancost, Alkenone
663   and boron-based Pliocene pCO_2 records. *Earth Planet. Sci. Lett.*, 2010. **292**: p. 201-211,

664   19.   Pagani, M., M.A. Authur, and K.H. Freeman, Miocene evolution of atmospheric carbon dioxide.
665   *Paleoceanography*, 1999. **14**: p. 273-292,

666   20.   Pagani, M., K.H. Freeman, and M.A. Arthur, Late Miocene atmospheric CO_2 concentrations and
667   the expansion of C-4 grasses. *Science*, 1999. **285**: p. 876-879,

668   21.   Pagani, M., M. Huber, Z.H. Liu, S. Bohaty, J. Henderiks, W. Sijp, S. Krishnan, and R. DeConto,
669   The role of carbon dioxide during the onset of Antarctic glaciation. *Science*, 2011. **334**: p.
670   1261-1264,

671   22.   Pagani, M., Z.H. Liu, J. LaRiviere, and A.C. Ravelo, High Earth-system climate sensitivity
672   determined from Pliocene carbon dioxide concentrations. *Nat. Geosci.*, 2010. **3**: p. 27-30, DOI:
673   10.1038/ngeo724.

674   23.   Bijl, P.K., A.J.P. Houben, S. Schouten, S. Bohaty, A. Sluijs, G.J. Reichart, J.S.S. Damste, and H.
675   Brinkhuis, Transient Middle Eocene atmospheric CO_2 and temperature variations. *Science*, 2010.
676   **330**: p. 819-821,

677   24.   Palmer, M.R., G.J. Brummer, M.J. Cooper, H. Elderfield, M.J. Greaves, G.J. Reichart, S.
678   Schouten, and J.M. Yu, Multi-proxy reconstruction of surface water pCO_2 in the northern Arabian
679   Sea since 29 ka. *Earth Planet. Sci. Lett.*, 2010. **295**: p. 49-57,

680   25.   Beerling, D.J. and D.L. Royer, Convergent Cenozoic CO_2 history. *Nat. Geosci.*, 2011. **4**: p.
681   418-420,

682   26.   Jasper, J.P. and J.M. Hayes, A carbon isotope record of CO_2 levels during the late Quaternary.
683   *Nature*, 1990. **347**: p. 462-464,

684   27.   Jasper, J.P., J.M. Hayes, A.C. Mix, and F.G. Prahl, Photosynthetic fractionation of ^{13}C and
685   concentrations of dissolved CO_2 in the central equatorial Pacific during the last 255,000 years.
686   *Paleoceanography*, 1994. **9**: p. 781-798,

687   28.   Pagani, M., J.C. Zachos, K.H. Freeman, B. Tipple, and S. Bohaty, Marked decline in atmospheric
688   carbon dioxide concentrations during the Paleogene. *Science*, 2005. **309**: p. 600-603, DOI:
689   10.1126/science.1110063.

690   29.   Conte, M., J.K. Volkman, and G. Eglinton, *Lipid biomarkers of the Haptophyta*, in *The
691   Haptophyte Algae*, J.C. Green and B.S.C. Leadbeater, Editors. 1994, Clarendon Press: Oxford. p.
692   351-377.

693   30.   Volkman, J.K., S.M. Barrett, S.I. Blackburn, and E.L. Sikes, Alkenones in *Gephyrocapsa
694   oceanica*: Implications for studies of paleoclimate. *Geochim. Cosmochim. Acta*, 1995. **59**: p.
695   513-520,

696   31.   McIntyre, A., *Gephyrocapsa protohyxleyi* sp. n. as possible phyletic link and index fossil for the
697   Pleistocene. *Deep Sea Res. I*, 1970. **17**: p. 187-190,

698   32.   Hay, W.W., *Calcareous nannofossils*, in *Oceanic Micropaleontology*, A.T.S. Ramsey, Editor 1977,
699   Academic Press: London, UK.

700   33.   Young, J., Size variation of Neogene *Reticulofenestra* coccoliths from Indian Ocean DSDP cores.
701   *J. Micropalaeontol.*, 1990. **9**: p. 71-85,

- 28 -

Page 29 of 39

Submitted to Phil. Trans. R. Soc. A - Issue

34. Marlowe, I.T., S.C. Brassell, G. Eglinton, and J.C. Green, Long-chain alkenones and alkyl alkenoates and the fossil coccolith record of marine sediments. *Chem. Geol.*, 1990. **88**: p. 349-375,

35. Young, J.R., *Neogene Calcareous Nannofossil Biostratigraphy*, P.R. Bown, Editor 1998, Springer Netherlands. p. 225-265.

36. Plancq, J., V. Grossi, J. Henderiks, L. Simon, and E. Mattioli, Alkenone producers during late Oligocene-early Miocene revisited. *Paleoceanography*, 2012. **27**, DOI: doi:10.1029/2011PA002164.

37. Henderiks, J. and M. Pagani, Refining ancient carbon dioxide estimates: Significance of coccolithophore cell size for alkenone-based pCO_2 records. *Paleoceanography*, 2007. **22**, DOI: doi:10.1029/2006PA001399.

38. Popp, B.N., F. Kenig, S.G. Wakeham, E.A. Laws, and R.R. Bidigare, Does growth rate affect ketone unsaturation and intracellular carbon isotopic variability in *Emiliania hyxleyi*? *Paleoceanography*, 1998. **13**: p. 35-41,

39. Farquhar, G.D., J.R. Ehleringer, and K.T. Hubick, Carbon isotope discrimination and photosynthesis. *Annu Rev Plant Physiol Plant Mol Biol*, 1989. **40**: p. 503-537,

40. Farquhar, G.D., M.H. O'Leary, and J.A. Berry, On the relationship between carbon isotope discrimination and the intercellular carbon dioxide concentration in leaves. *Aust. J. Plant Physiol.*, 1982. **9**: p. 121-137,

41. Goericke, R., J.P. Montoya, and B. Fry, *Physiology of isotope fractionation in algae and cyanobateria*, in *Stable isotope in ecology*, K. Lajtha and B. Michener, Editors. 1994, Blackwell Scientific: Cambridge.

42. Popp, B.N., E.A. Laws, R.R. Bidigare, J.E. Dore, K.L. Hanson, and S.G. Wakeham, Effect of Phytoplankton Cell Geometry on Carbon Isotopic Fractionation. *Geochim. Cosmochim. Acta*, 1998. **62**: p. 69-77, DOI: doi:10.1016/s0016-7037(97)00333-5.

43. Laws, E.A., B.N. Popp, R.R. Bidigare, M.C. Kennicutt, and S.A. Macko, Dependence of phytoplankton carbon isotopic composition on growth rate and $[CO_2]aq$: Theoretical considerations and experimental results. *Geochim. Cosmochim. Acta*, 1995. **59**: p. 1131-1138, DOI: 10.1016/0016-7037(95)00030-4.

44. Laws, E.A., R.R. Bidigare, and B.N. Popp, Effect of growth rate and CO_2 concentration on carbon isotopic fractionation by the marine diatom *Phaeodactylum tricornutum. Limnol. Oceanogr.*, 1997. **42**: p. 1552-1560,

45. Riebesell, U., A.T. Revill, D.G. Holdsworth, and J.K. Volkman, The effects of varying CO_2 concentration on lipid composition and carbon isotope fractionation in *Emiliania huxleyi*. *Geochim. Cosmochim. Acta*, 2000. **64**: p. 4179-4192, DOI: 10.1016/s0016-7037(00)00474-9.

46. Rost, B., I. Zondervan, and U. Riebesell, Light-dependent carbon isotope fractionation in the coccolithophorid *Emiliania huxleyi. Limnol. Oceanogr.*, 2002. **47**: p. 120-128,

47. Burkhardt, S., U. Riebesell, and I. Zondervan, Effects of growth rate, CO_2 concentration, and cell size on the stable carbon isotope fractionation in marine phytoplankton. *Geochim. Cosmochim. Acta*, 1999. **63**: p. 3729-3741, DOI: 10.1016/s0016-7037(99)00217-3.

48. Raven, J.A. and A.M. Johnston, Mechanisms of inorganic-carbon acquisition in marine phytoplankton and their implications for the use of other resources. *Limnol. Oceanogr.*, 1991. **36**:

743   p. 1701-1714,

744   49.   Raven, J.A., A.M. Johnston, and D.H. Turpin, Influence of changes in CO_2 concentration and

745   temperature on marine phytoplankton 13C/12C ratios: an analysis of possible mechanisms. *Global*

746   *Planet. Change*, 1993. **8**: p. 1-12, DOI: 10.1016/0921-8181(93)90058-v.

747   50.   Laws, E.A., B.N. Popp, N. Cassar, and J. Tanimoto, ^{13}C discrimination patterns in oceanic

748   phytoplankton: likely influence of CO_2 concentrating mechanisms, and implications for

749   palaeoreconstructions. *Funct. Plant Biol.*, 2002. **29**: p. 323-333,

750   51.   Giordano, M., J. Beardall, and J.A. Raven, CO_2 concentrating mechanisms in algae: Mechanisms,

751   environmental modulation, and evolution. *Annu. Rev. Plant Biol.*, 2005. **56**: p. 99-131,

752   52.   Rau, G.H., U. Riebesell, and D. Wolf-Gladrow, A model of photosynthetic C-13 fractionation by

753   marine phytoplankton based on diffusive molecular CO2 uptake. *Mar. Ecol.-Prog. Ser.*, 1996. **133**:

754   p. 275-285, DOI: 10.3354/meps133275.

755   53.   Bidigare, R.R., et al., Consistent fractionation of 13C in nature and in the laboratory: Growth-rate

756   effects in some haptophyte algae. *Global Biogeochem. Cyc.*, 1997. **11**: p. 279-292, DOI:

757   doi:10.1029/96GB03939.

758   54.   Shipboard Scientific Party, *Site 925*, in *Proceedings of the Ocean Drilling Program, Initial*

759   *Reports*, W.B. Curry, N.J. Shackleton, and C. Richter, Editors. 1995, Ocean Drilling Program:

760   College Station, TX.

761   55.   Conkright, M.E., R.A. Locarnini, H.E. Garcia, T.D. O'Brien, T.P. Boyer, C. Stephens, and J.I.

762   Antonov, *World Ocean Atlas 2001: Objective analyses, data statistics, and figures*, 2002, National

763   Oceanographic Data Center: Silver Springs, MD.

764   56.   Hay, W.W., et al., *An alternative global Cretaceous paleogeography*, in *The evolution of*

765   *Cretaceous ocean/climate systems*, E. Barrera and C. Johnson, Editors. 1999, Geological Society

766   of America: Boulder, CO. p. 1-48.

767   57.   Nilsen, E.B., L.D. Anderson, and M.L. Delaney, Paleoproductivity, nutrient burial, climate change

768   and the carbon cycle in the western equatorial Atlantic across the Eocene/Oligocene doundary.

769   *Paleoceanography*, 2003. **18**, DOI: doi:10.1029/2002PA000804.

770   58.   Takahashi, T., et al., Climatological mean and decadal change in surface ocean pCO2, and net

771   sea–air CO2 flux over the global oceans. *Deap-Sea Res. II*, 2009. **56**: p. 554-577, DOI:

772   10.1016/j.dsr2.2008.12.009.

773   59.   Prahl, F.G. and S.G. Wakeham, Calibration of unsaturation patterns in long-chain ketone

774   compositions for palaeotemperature assessment. *Nature*, 1987. **330**: p. 367-369,

775   60.   Brassell, S.C., G. Eglinton, I.T. Marlowe, U. Pflaumann, and M. Sarnthein, Molecular stratigraphy:

776   a new tool for climatic assessment. *Nature*, 1986. **320**: p. 129-133,

777   61.   Hopmans, E.C., S. Schouten, R.D. Pancost, M.T.J. van der Meer, and J.S. Sinnighe Damste,

778   Analysis of intact tetraether lipids in archaeal cell material and sediments by high performance

779   liquid chromatography/atmospheric pressure chemical ionization mass spectrometry. *Rapid*

780   *Commun. Mass Spectrom.*, 2000. **14**: p. 585-589,

781   62.   Schouten, S., E.C. Hopmans, E. Schefuss, and J.S.S. Damste, Distributional variations in marine

782   crenarchaeotal membrane lipids: a new tool for reconstructing ancient sea water temperatures?

783   *Earth Planet. Sci. Lett.*, 2002. **204**: p. 265-274,

- 30 -

Page 31 of 39

Submitted to Phil. Trans. R. Soc. A - Issue

784 63. Pearson, P.N. and W.P. Chaisson, *Late Paleocene to middle Miocene planktonic foraminifer*
785 *biostratigraphy of the Ceara Rise*, in *Proceedings of the Ocean Drilling Program, Scienfitic*
786 *Results*, N.J. Shackleton, W.B. Curry, R.A. Richards, and T.J. Bralower, Editors. 1997, Ocean
787 Drilling Program: College Station, TX.

788 64. Chaisson, W.P. and P.N. Pearson, *Planktonic foraminifer biostratigraphy at Site 925: Middle*
789 *Miocene-Pleistocene*, in *Proceedings of the Ocean Drilling Program, Scientific Results*, N.J.
790 Shackleton, W.B. Curry, C. Richter, and T.J. Bralower, Editors. 1997, Ocean Drilling Program:
791 College Station, TX.

792 65. Cande, S.C. and D.V. Kent, Revised calibration of the geomagnetic polarity timescale for the late
793 Cretaceous and Cenozoic. *J. Geophys. Res.*, 1995. **100**: p. 6093-6095,

794 66. Berggren, W.A., D.V. Kent, C.C. Swisher, and M.-P. Aubry, *A revised Cenozoic geochronology*
795 *and chronostratigraphy*, in *Geochronology, time scales and global stratigraphic correlation*, W.A.
796 Berggren, D.V. Kent, M.-P. Aubry, and J. Hardenbol, Editors. 1995, SEPM Society for
797 Sedimentary Geology: Tulsa, OK. p. 129-212.

798 67. Conte, M., M.-A. Sicre, and C. Ruhlemann, Global temperature calibration of the alkenone
799 unsaturation index ($U^{K'}_{37}$) in surface waters and comparison with surface sediments. *Geochem.*
800 *Geophys. Geosyst.*, 2006. **7**, DOI: doi:10.1029/2005GC001054.

801 68. Liu, Z., M. Pagani, D. Zinniker, R. DeConto, M. Huber, H. Brinkhuis, S.R. Shah, R.M. Leckie,
802 and A. Pearson, Global Cooling During the Eocene-Oligocene Climate Transition. *Science*, 2009.
803 **323**: p. 1187-1190, DOI: 10.1126/science.1166368.

804 69. Hopmans, E.C., J.W.H. Weijers, E. Schefuß, L. Herfort, J.S. Sinninghe Damsté, and S. Schouten,
805 A novel proxy for terrestrial organic matter in sediments based on branched and isoprenoid
806 tetraether lipids. *Earth Planet. Sci. Lett.*, 2004. **224**: p. 107-116,

807 70. Spero, H.J., K.M. Mielke, E.M. Kalve, D.W. Lea, and D.K. Pak, Multispecies approach to
808 reconstructing eastern equatorial Pacific thermocline hydrography during the past 360 kyr.
809 *Paleoceanography*, 2003. **18**, DOI: doi:10.1029/2002PA000814.

810 71. DeConto, R. and D. Pollard, Rapid Cenozoic glaciation of Antarctica induced by declining
811 atmospheric CO_2. *Nature*, 2003. **421**: p. 245-249,

812 72. DeConto, R.M., D. Pollard, P.A. Wilson, H. Palike, C.H. Lear, and M. Pagani, Thresholds for
813 Cenozoic bipolar glaciation. *Nature*, 2008. **455**: p. 652-U52, DOI: 10.1038/nature07337.

814 73. Knauss, J.A., *Introduction to Physical Oceanography*. 2nd ed 2006, Long Grove, IL: Waveland
815 Press. 309.

816 74. Palike, H., R.D. Norris, J.O. Herrle, P.A. Wilson, H.K. Coxall, C.H. Lear, N.J. Shackleton, A.
817 Tripati, and B.S. Wade, The heartbeat of the Oligocene climate system. *Science*, 2006. **314**: p.
818 1894-1898,

819 75. Zachos, J.C., G.R. Dickens, and R.E. Zeebe, An early Cenozoic perspective on greenhouse
820 warming and carbon-cycle dynamics. *Nature*, 2008. **451**: p. 279-283,

821 76. Miller, K.G., J.D. Wright, and R.G. Fairbanks, Unlocking the ice house: Oligocene to Miocene
822 oxygen isotopes eustasy and margin erosion. *J. Geophys. Res.*, 1991. **96**: p. 6829-6848,

823 77. Lear, C.H., Y. Rosenthal, H.K. Coxall, and P.A. Wilson, Late Eocene to early Miocene ice sheet
824 dynamics and the global carbon cycle. *Paleoceanography*, 2004. **19**, DOI:

Submitted to Phil. Trans. R. Soc. A - Issue

Page 32 of 39

825   10.1029/2004PA001039.

826 78. Pollard, D. and R.M. DeConto, Hysteresis in Cenozoic Antarctic ice-sheet variations. *Global*
827   *Planet. Change*, 2005. **45**: p. 9-21,

828 79. Hague, A.M., D.J. Thomas, M. Huber, R. Korty, S.C. Woodard, and L.B. Jones, Convection of
829   North Pacific deep water during the early Cenozoic. *Geology*, 2012. **40**: p. 527-530,

830 80. Thomas, D.J., M. Lyle, T.C. Moore Jr., and D.K. Rea, Paleogene deepwater mass composition of
831   the tropical Pacific and implications for thermohaline circulation in a greenhouse world. *Geochem.*
832   *Geophys. Geosyst.*, 2008. **9**, DOI: doi:10.1029/2007GC001748.

833 81. Pearson, P.N. and M.R. Palmer, Atmospheric carbon dioxide concentrations over the past 60
834   million years. *Nature*, 2000. **406**: p. 695-699,

835 82. Lunt, D.J., G.L. Foster, A.M. Haywood, and E.J. Stone, Late Pliocene Greenland glaciation
836   controlled by a decline in atmospheric CO_2 levels. *Nature*, 2008. **454**: p. 1102-U41, DOI:
837   10.1038/nature07223.

838 83. Ruddiman, W.F., A paleoclimatic enigma? *Science*, 2010. **328**: p. 838-839,

839 84. LaRiviere, J.P., A.C. Ravelo, A. Crimmins, P.S. Dekens, H.L. Ford, M. Lyle, and M.W. Wara,
840   Late Miocene decoupling of oceanic warmth and atmospheric carbon dioxide forcing. *Nature*,
841   2012. **486**: p. 97-100,

842 85. You, Y., M. Huber, R.D. Muller, C.J. Poulsen, and J. Ribbe, Simulation of the Middle Miocene
843   Climate Optimum. *Geophys. Res. Lett.*, 2009. **36**, DOI: doi:10.1029/2008GL036571.

844 86. Holbourn, A., W. Kuhnt, M. Schulz, and H. Erlenkeuser, Impacts of orbital forcing and
845   atmospheric carbon dioxide on Miocene ice-sheet expansion. *Nature*, 2005. **438**: p. 483-487,

846 87. Badger, M.R., T.J. Andrews, S.M. Whitney, M. Ludwig, D.C. Yellowlees, W. Leggat, and G.D.
847   Price, The diversity and coevolution of Rubisco, plastids, pyrenoids, and chloroplast-based
848   CO_2-concentrating mechanisms in algae. *Canad. J. Bot.*, 1998. **76**: p. 1052-1071,

849 88. Rickaby, R.E.M., J. Henderiks, and J.N. Young, Perturbing phytoplankton: response and isotopic
850   fractionation with changing carbonate chemistry in two coccolithophore species. *Clim. Past*, 2010.
851   **6**: p. 771-785,

852 89. Henderiks, J. and M. Pagani, Coccolithophore cell size and the Paleogene decline in atmospheric
853   CO_2. *Earth Planet. Sci. Lett.*, 2008. **269**: p. 575-583,

854 90. Riebesell, U., D.A. Wolf-Gladrow, and V. Smetacek, Carbon dioxide limitation of marine
855   phytoplankton growth rates. *Nature*, 1993. **361**: p. 249-251,

856 91. Wolf-Gladrow, D. and U. Riebesell, Diffusion and reactions in the vicinity of plankton: A refined
857   model for inorganic carbon transport. *Mar. Chem.*, 1997. **59**: p. 17-34,

858 92. Jahne, B., G. Heinz, and W. Dietrich, Measurement of the diffusion coefficents of sparingly
859   soluble gases in water *J. Geophys. Res.*, 1987. **92**: p. 10767-10776,

860 93. Gavis, J. and J.F. Ferguson, Kinetics of carbon dioxide uptake by phytoplankton at high pH.
861   *Limnol. Oceanogr.*, 1975. **20**: p. 211-221,

862 94. Dickson, A.G. and C. Goyet, *Handbook of method for the analysis of the various parameters of*
863   *the carbon dioxide system in sea water*, 1994, Department of Energy: ORNL-CDIAC-74.

864 95. Kameo, K.T. and T.J. Bralower, *Size variation of reticulofenestra coccoliths during the Neogene*,
865   in *Proceedings of the Ocean Drilling Program - Scientific Results*, R.M. Leckie and J. Sigurdsson,

866   Editors. 2000, Ocean Drilling Program: College Station, TX. p. 3-17.

867   96.   Pagani, M., *Biomarker-based inferences of past climate: The alkenone pCO$_2$ proxy*, in *Treatise on*
868   *Geochemistry*, H.D. Holland and K.K. Turekian, Editors. 2013, Elsevier: Amsterdam, The
869   Netherlands, in press.

870   97.   Popp, B.N., R.R. Bidigare, B. Deschenes, E.A. Laws, F.G. Prahl, J. Tanimoto, and R.J.
871   Wallsgrove, A new method for estimating growth rates of alkeone-producing haptophytes. *Limnol.*
872   *Oceanogr.: Meth.*, 2006. **4**,

873

874
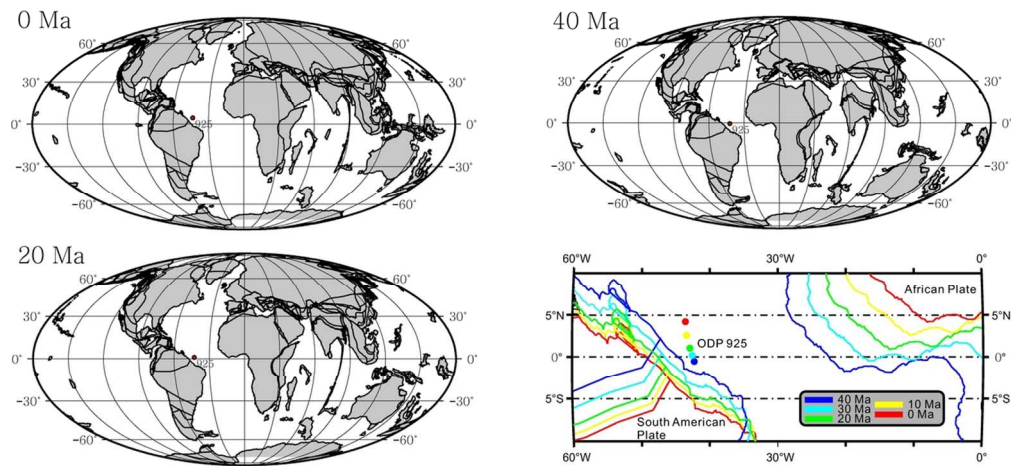
Global plate reconstruction shows the location of ODP Site 925 at 40 Ma, 20 Ma, and the present, as well as a detail of the northward movement of Site 925 since 40 Ma [56]. Continents are shown as tectonic terrains rather than shorelines.
112x51mm (300 x 300 DPI)

1
2
3
4
5
6
7
8
9
10
11
12
13
14
15
16
17
18
19
20
21
22
23
24
25
26
27
28
29
30
31
32
33
34
35
36
37
38
39
40
41
42
43
44
45
46
47
48
49
50
51
52
53
54
55
56
57
58
59
60
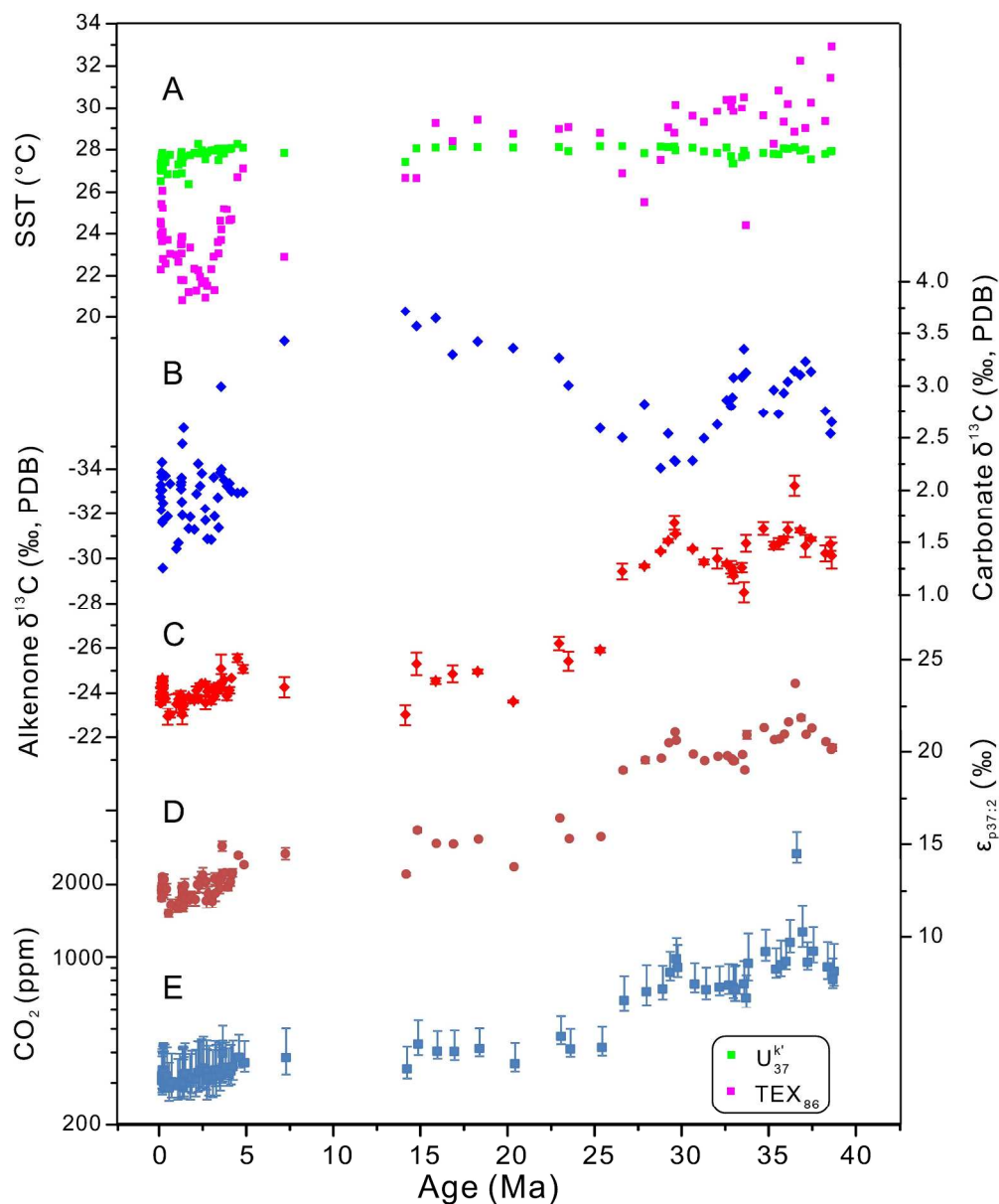
Time series of ODP Site 925. (A) $U^{k'}_{37}$ and TEX_{86} based SST reconstruction; (B) Adjusted carbon isotopes from foraminiferal stable isotope measurements to proximate $\delta^{13}C$ of surface water dissolved inorganic carbon. (C) Carbon isotopes of alkenones; (D) $\varepsilon_{p37:2}$ calculated from (B) and (C); (E) pCO_2 calculated from (D), using both $U^{k'}_{37}$ and TEX_{86} based SST estimates, and assuming $[PO_4^{3-}]$ values were 0.20, 0.14 (lower limit) and 0.39 μM (upper limit). Refer to Supplementary Material to see details of constructing (B), (D), (E) and their related uncertainties; One CO_2 estimate at 35.52 Ma give value > 2400 ppm, which is off the chart and therefore not shown in the following figures.
235x284mm (300 x 300 DPI)

Submitted to Phil. Trans. R. Soc. A - Issue

Page 36 of 39

1
2
3
4
5
6
7
8
9
10
11
12
13
14
15
16
17
18
19
20
21
22
23
24
25
26
27
28
29
30
31
32
33
34
35
36
37
38
39
40
41
42
43
44
45
46
47
48
49
50
51
52
53
54
55
56
57
58
59
60
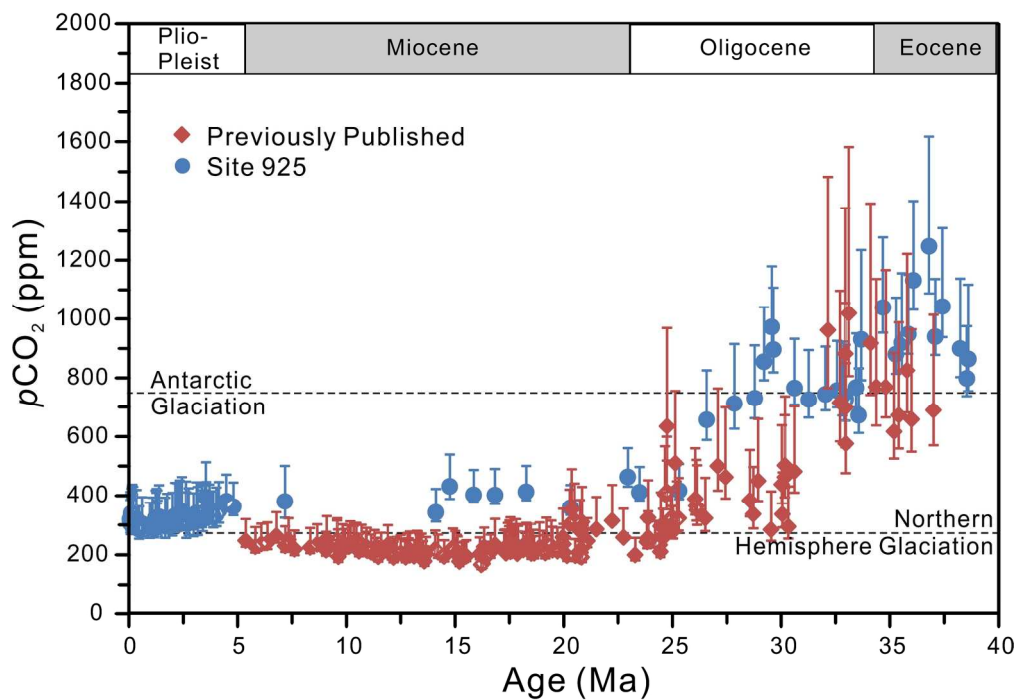
A comparison of alkenone-based pCO_2 composite from multiple marine sites as compiled in [28] and ODP Site 925 record since the late Eocene. Antarctic glaciation thresholds (~750 ppm) and Northern Hemisphere glaciation threshold (~280 ppm) deduced from climate models [72] are marked by dashed lines.
172x118mm (300 x 300 DPI)

Page 37 of 39

Submitted to Phil. Trans. R. Soc. A - Issue

1
2
3
4
5
6
7
8
9
10
11
12
13
14
15
16
17
18
19
20
21
22
23
24
25
26
27
28
29
30
31
32
33
34
35
36
37
38
39
40
41
42
43
44
45
46
47
48
49
50
51
52
53
54
55
56
57
58
59
60
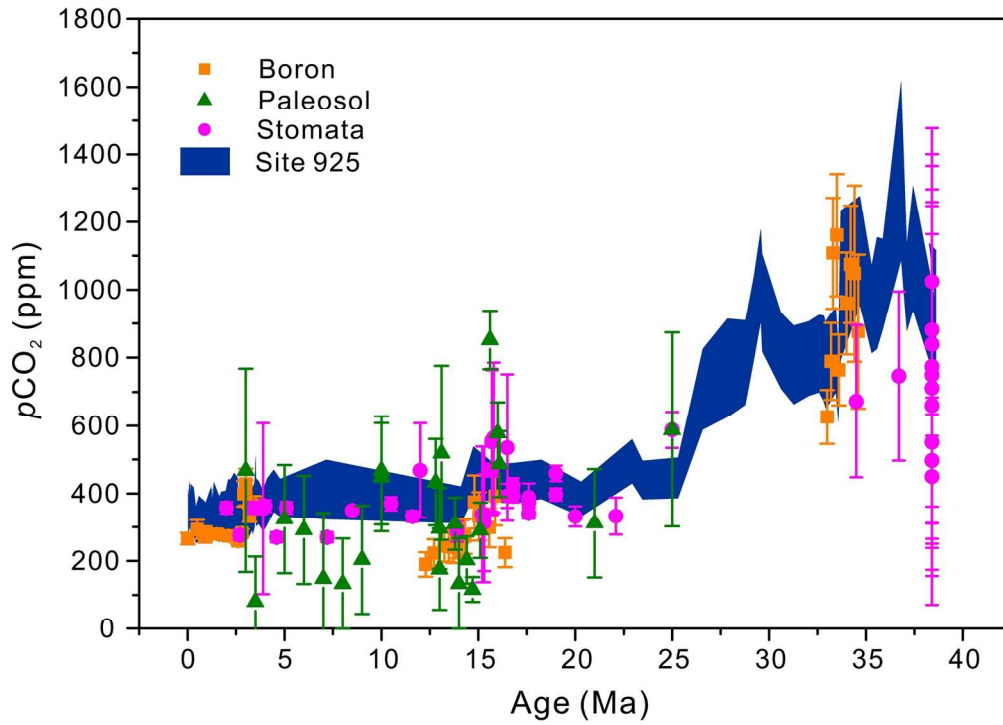
Comparison between different proxy-based pCO_2 estimates for the past 40 Ma. Boron isotope, paleosol and stomata data are summarized by [25], with additional data from Foster et al. (2012) [15].
170x121mm (300 x 300 DPI)
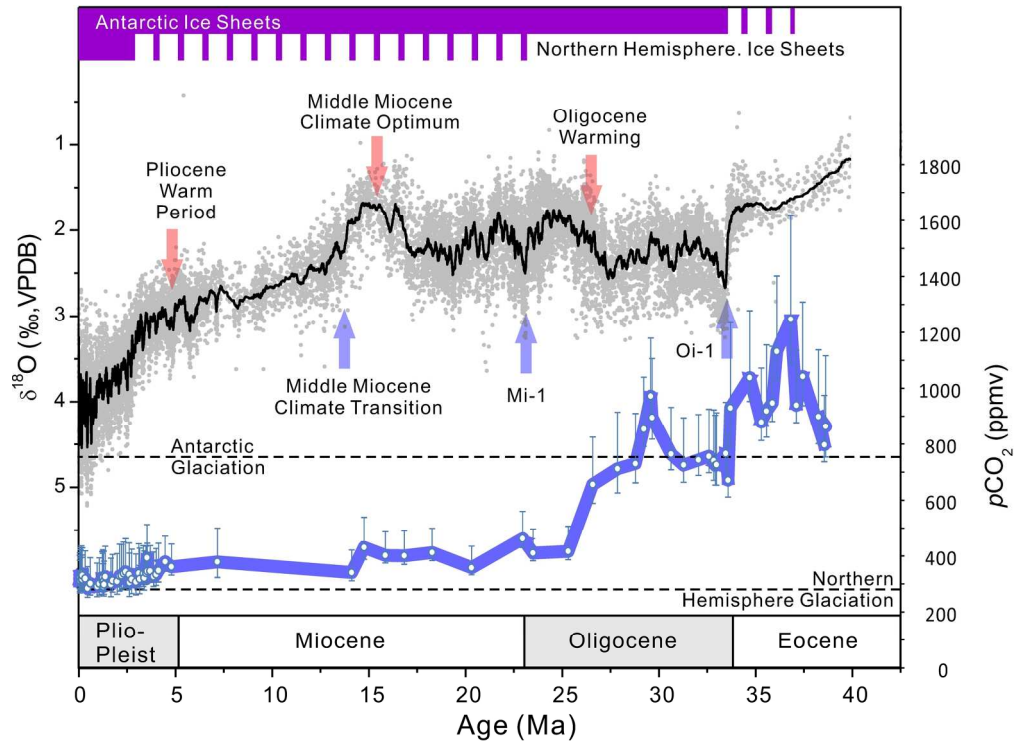
Climate and atmospheric CO_2 history for the past 40 Ma. Benthic $\delta^{18}O$ from [75]. Major warming (red arrows) and cooling (blue arrows) events are labeled. Red bars indicate brief history of Antarctic and Northern Hemisphere ice sheets. Antarctic glaciation thresholds (~750 ppm) and Northern Hemisphere glaciation threshold (~280 ppm) deduced from climate models [72] are marked by dashed lines. 190x139mm (300 x 300 DPI)

Page 39 of 39

Submitted to Phil. Trans. R. Soc. A - Issue

1
2
3
4
5
6
7
8
9
10
11
12
13
14
15
16
17
18
19
20
21
22
23
24
25
26
27
28
29
30
31
32
33
34
35
36
37
38
39
40
41
42
43
44
45
46
47
48
49
50
51
52
53
54
55
56
57
58
59
60
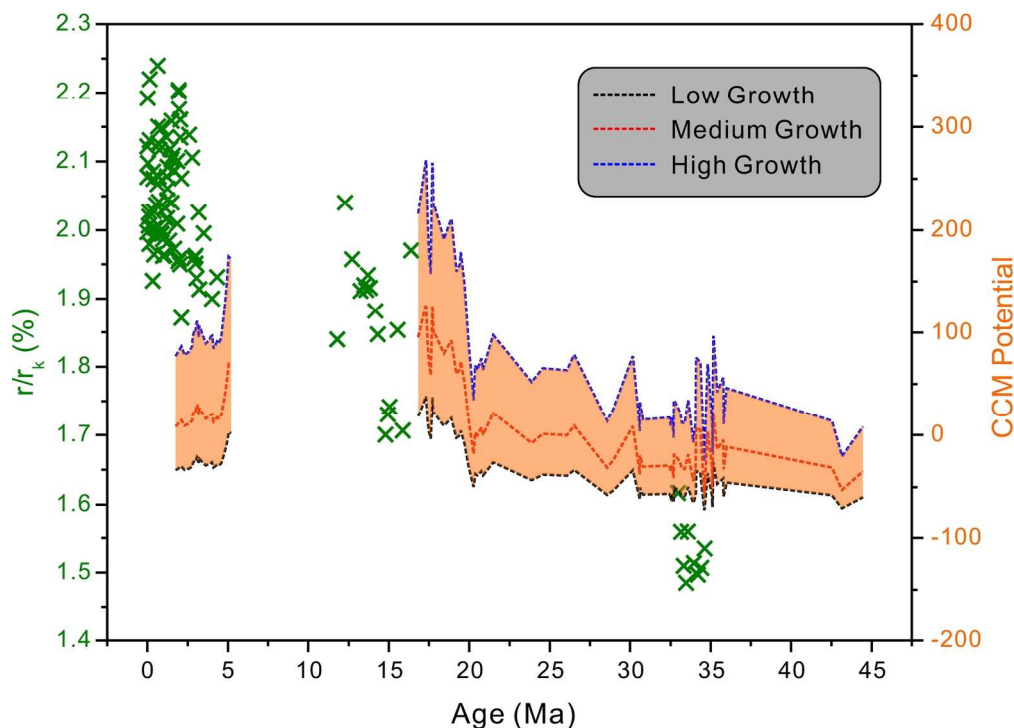
Comparison between the spontaneous bicarbonate-$CO_{2(aq)}$ conversion (green symbols) and the CCM potential of alkenone producers (orange bands) for the past 45 Ma. HCO_3^--$CO_{2(aq)}$ conversion (r/r_k) based on the model of Riebesell et al. (1993) and Wolf-Gladrow et al., (1997) [90, 91], using seawater pH and SST data provided by boron isotope studies [13, 15, 16, 18], and a constant radius of 2.67 µm for alkenone-producing haptophyte algae. Computation of CCM potential is based on the model of [44, 50], utilizing previously published cell size [21, 37, 89, 95] and existing paleo-CO2 estimates [18, 21, 28]. CCM potential ($[(µ/C_e)/(/P/C)]100 − 100$) represents an arbitrary, qualitative scale of CCM activity.
165x121mm (300 x 300 DPI)